

Tuning into spatial frequency space

Satellite and space debris detection in the ZTF alert stream.

J. P. Carvajal^{1,2,*}, F. E. Bauer^{1,2,3}, I. Reyes-Jainaga⁴, F. Förster^{2,5,6}, A. M. Muñoz Arancibia^{2,5}, M. Cateñan^{1,2,7}, P. Sánchez-Sáez^{8,2}, C. Ricci^{9,10}, and A. Bayo⁸

¹ Instituto de Astrofísica, Pontificia Universidad Católica de Chile, Av. Vicuña Mackenna 4860, 7820436 Macul, Santiago, Chile

² Millennium Institute of Astrophysics (MAS), Nuncio Monsenor Sotero Sanz 100, Providencia, Santiago, Chile

³ Space Science Institute, 4750 Walnut Street, Suite 205, Boulder, Colorado 80301, USA

⁴ Data Observatory, Av. Eliodoro Yáñez 2990, oficina A5, Providencia, Chile

⁵ Center for Mathematical Modeling (CMM), University of Chile, AFB170001, Santiago, Chile

⁶ Data & Artificial Intelligence Initiative (ID&IA), University of Chile, Santiago, Chile

⁷ Centro de Astro-Ingeniería, Pontificia Universidad Católica de Chile, Av. Vicuña Mackenna 4860, 7820436 Macul, Santiago, Chile

⁸ European Southern Observatory, Karl-Schwarzschild-Strasse 2, 85748 Garching bei München, Germany

⁹ Instituto de Estudios Astrofísicos, Facultad de Ingeniería y Ciencias, Universidad Diego Portales, Av. Ejército Libertador 441, Santiago, Chile

¹⁰ Kavli Institute for Astronomy and Astrophysics, Peking University, Beijing 100871, China

Received September 15, 1996; accepted March 16, 1997

ABSTRACT

Context. A significant challenge in the study of transient astrophysical phenomena is the identification of bogus events, among which human-made Earth-orbiting satellites and debris remain a key contaminant. Existing pipelines effectively identify satellite trails but can miss more complex signatures, such as collections of dots known as satellite glints. In the Rubin Observatory era, the scale of the operations will increase tenfold with respect to its precursor, the Zwicky Transient Facility (ZTF), requiring crucial improvements in classification purity, data compression for informative alerts, pipeline speed and other areas.

Aims. We explore the use of the 2D Fast Fourier Transform (FFT) on difference images as a tool to improve satellite detection machine learning algorithms.

Methods. Adopting the single-stamp classification model from the Automatic Learning for the Rapid Classification of Events (ALeRCE) broker as a baseline, we adapt its architecture to receive a cutout of the FFT of the difference image, in addition to the three (science, reference, difference) ZTF image cutouts (hereafter stamps). We study different stamp sizes and resolutions for these four channels, aiming to assess the benefit of including the FFT image, particularly in scenarios where data compression remains essential due to alert size limitations and pipeline processing speed requirements (e.g., for surveys like the Legacy Survey of Space and Time).

Results. The inclusion of the FFT improved satellite detection accuracy, with the most notable increase observed in the model with the smallest field of view (16''), where accuracy rose from 66.9% to 79.7% (a statistically significant improvement of $\approx 13\%$ with a 95% confidence interval of 7.8% to 17.8%). This result demonstrates the effectiveness of FFT in compressing relevant information and extracting features that characterize satellite signatures in larger difference images.

Conclusions. We show how FFTs can be leveraged to cull satellite and space debris signatures from alert streams.

Key words. Techniques: image processing – Techniques: photometric – Methods: data analysis – Surveys.

1. Introduction

Large étendue telescopes engaging in time-domain surveys, such as the Zwicky Transient Facility (ZTF, Bellm et al. 2018; Graham et al. 2019), have quickly become a cornerstone of observational astrophysics. ZTF has revolutionized our ability to detect and characterize a wide variety of transients, active galaxies, and variable star phenomena (e.g., Chen et al. 2020; Perley et al. 2020; Carrasco-Davis et al. 2021; Sánchez-Sáez et al. 2021, 2023), through both its 5- σ difference-image alert stream and frequent data releases (Masci et al. 2019). Overall, ZTF distributes up to 10^6 alerts each night (with a median closer to $\sim 200\,000$) which equates to tens of GBs of data per night (Paterson et al. 2018). The expected rates for the Legacy Survey

of Space and Time (LSST, LSST Science Collaboration et al. 2009; Ivezić et al. 2019) from the Vera C. Rubin Observatory will be an order of magnitude larger, with a single-visit depth almost 4 magnitudes deeper in the r band compared to ZTF. A handful of so-called community alert brokers have dedicated themselves to the distribution, filtering, and annotation of these massive alert volumes. These brokers ingest the alert streams and provide processed science products and services that enable the community to pursue their science goals without overloading the observatories' infrastructure. Current full-stream community brokers for ZTF and future LSST include ALeRCE (Förster et al. 2021), AMPEL (Nordin et al. 2019), ANTARES (Matheson et al. 2021), Babamul, Fink (Möller et al. 2020), Lasair (Smith et al. 2019), and Pitt-Google¹.

* Corresponding author: Jcarvajal000@gmail.com

¹ <https://pitt-broker.readthedocs.io/en/latest/>

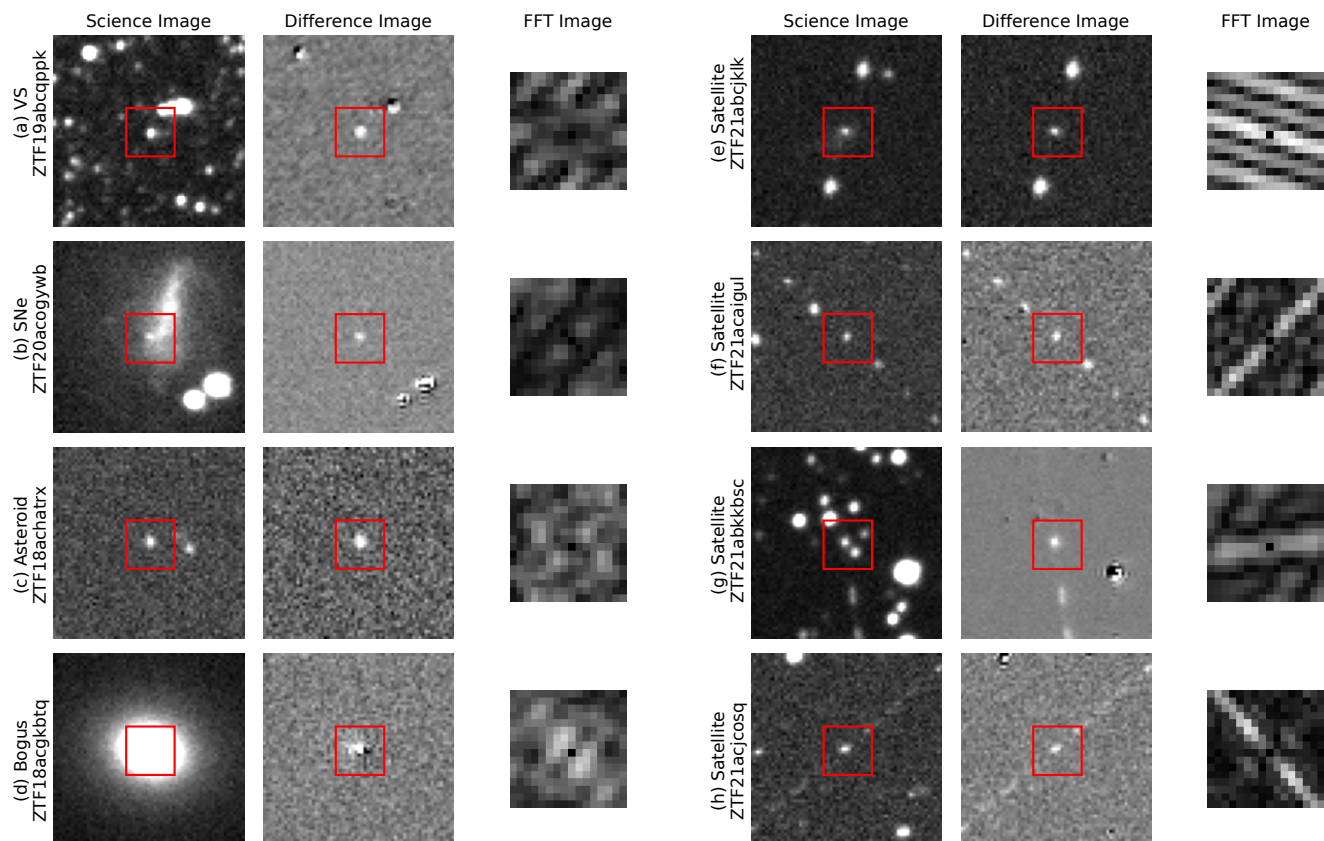


Fig. 1: Comparison of science image, difference image, and its FFT for various transient sources and contaminants in the ZTF alert stream. The full $63'' \times 63''$ science and difference stamps are shown, with the central $16'' \times 16''$ denoted in red. The FFT image stamp is cropped into the central 16×16 pixels. Panels (a)-(c) display astrophysical events: (a) variable star ZTF19abcpppk; (b) supernova ZTF20acogywb; and (c) asteroid ZTF18achatr. Panel (d) shows a typical bogus event (ZTF18acgkbtq), characteristic of a bad subtraction. Panels (e)-(h) highlight different types of satellite signatures that reached the alert stream: (e) and (f), from alerts ZTF21abcjklk and ZTF21acaigul, show the typical regular glint signature with different separation among glints; (g) shows a satellite with irregular glints and an overall asymmetric signature; (h) shows a satellite with both a continuous signature and glints. This small portion of Fourier space effectively captures the distinct extended signals of satellites.

One of the persistent challenges is the identification and removal of contaminants (often referred to as “bogus” detections) from the observations and the transient event alert stream. Mitigation of bogus events is particularly important for robust early transient discovery and classification, such as identifying flash-ionization episodes in young supernovae (SNe) or short-lived kilonovae; this was a prime motivation for the development of the real-time first-stamp classifier by ALerCE (Carrasco-Davis et al. 2021, hereafter, the “Stamp Classifier”). Notably, human-made satellites and space debris orbiting Earth can be particularly complicated contaminants to identify in real-time for existing algorithms and pipelines. Karpov & Peloton (2022, 2023) quantified the effect of *satellite glints* (see Fig. 1) that bypassed both the streak masking algorithm (Laher et al. 2014) and real-bogus classifier (Duev et al. 2019a) components of ZTF’s pipeline (Masci et al. 2019), finding at least ≈ 3000 glint-related alerts per month. For reference, this is ≈ 4.4 times the monthly rate of new transients detected by ZTF and reported to the Transient Name Server (TNS)².

This challenge is already a significant in the ZTF real-time alert stream and stands to become even more problematic in the LSST era due to the shift in stamp field of view (FoV), which

is slated to go from $63'' \times 63''$ at a $1''/\text{pixel}$ resolution for ZTF (e.g., Fig. 1) to $6'' \times 6''$ at a $0.2''/\text{pixel}$ resolution for LSST, due to bandwidth limitations associated with increased image resolution. An upside of the increased resolution is highlighted in recent work by Tyson et al. (2024), which shows how glints from tumbling low-Earth orbit debris may become identifiable due to distinct defocus and shape characteristics. This, however, does not completely alleviate the concerns, as glint-producing satellites occupy a wide range of orbits (Karpov & Peloton 2023). As discussed in Reyes-Jainaga et al. (2023, hereafter RJ23), a promising approach to mitigate the FoV reduction in LSST is to employ multiscale image stamps. These stamps capture a larger FoV with decreasing spatial resolution as the distance from the source center increases, effectively compressing data by preserving high-detail information in the central region while also retaining relevant contextual information, such as flux from satellite trails, around the alert.

Motivated by the potential for image compression and by the unique glint signatures of satellites and space debris (hereafter, simply “satellites”), we explore the spatial frequency domain of the difference images via the Fast Fourier Transform (FFT) algorithm (Cooley & Tukey 1965). Satellite glints, presumably caused by rotating objects that reflect sunlight, exhibit a range of patterns from simple (e.g., Fig. 1 (f)) to complex (e.g.,

² <https://www.wis-tns.org/>

Fig. 1 (g)). Additionally, multiple glints from a single satellite may not be captured within the FoV of a single stamp (e.g., see Sect. 4.2). These glints generally consist of a periodic signal, dominated by the satellite’s rotation, aligned along an approximately straight line within the locality of the image. The signal is convolved with the Point Spread Function (PSF), and under this locality approximation, we can assume a relatively constant illumination geometry. Therefore, inspecting the spatial frequencies of these satellite glint variations is a natural path to explore. Central, point-like emission maps to very extended scales in Fourier space, while extended emission maps to more compact scales. Thus, in contrast with the multiscale approach of RJ23, the central portions of the Fourier map naturally tap into the extended emission, while imaging cropping effectively limits the minimum scales probed, rather than the maximum ones.

Building upon the approach in RJ23, we analyze the effect of including FFT information within the adapted architecture of the ALerCE Stamp Classifier. The incorporation of the FFT slightly increases the model’s input size³, but we aim to assess its potential for capturing extended spatial features in a compact form. We present the methods and results in Sects. 2 and 3, respectively. In Sect. 4 we analyze the results and discuss the future prospects for the FFT, and how it can efficiently expand opportunities for improving streak detection algorithms (e.g., Duev et al. 2019b) to perform better on satellite glints while keeping inputs small, which will be fundamental in the LSST era both for internal pipelines and downstream filtering.

2. Enhancing the ALerCE Stamp Classifier with FFT

The ALerCE Stamp Classifier was first introduced in Carrasco-Davis et al. (2021), adopting a Convolutional Neural Network (CNN) model that classifies individual ZTF alerts based on three-channel image cutouts (science, reference, and difference) and additional metadata (e.g., coordinates, flux and magnitude measurements, and seeing) into four distinct astrophysical sources and bogus. The effectiveness of this machine learning (ML) model is demonstrated by ALerCE’s position as one of the top three reporting groups of transients to TNS, with $\lesssim 1\%$ contamination among spectroscopically classified transients first reported by Förster et al. (2021).

In this work, we explore the effect of incorporating FFTs in the Stamp Classifier, building upon previous works. Our modifications start from the model architecture introduced in RJ23, where the Satellite class was first introduced. The classifier categorizes alerts into six distinct classes: supernovae (SNe), variable stars, asteroids, active galactic nuclei (AGN), satellites, and bogus detections.

2.1. Preprocessing

After the ingestion of each alert, a preprocessing step takes place before the model run. A schematic is shown in Fig. 2. The detailed steps to go from the base ZTF stamps to the cropped stamp cube (blue box in the schematic), that serves as input for the model, are the following:

1. In the rare cases where the stamps do not have the original dimensions of 63×63 pixels (e.g., the object is by the edge of the CCD), the alert is dropped. The current necessity for

³ For example, for a central 16×16 px portion, this results in 128 floats ($16 \times 16 \div 2$, due to the complex conjugate symmetry of the FFT).

the source to lie in the center of the stamp complicates such modifications. An attempt to “repair” these cases has yet to be implemented.

2. In each of the stamps, a boolean integrity mask is constructed, where infinite and NaN (Not a Number) values in the stamp are associated with a True (1), and finite values with a False (0).
3. The non-finite values in the masked stamp are then set to zero (0).
4. For computational optimization, the normalization is performed in batches for each type of stamp. The maximum for the normalization is the 99th percentile of the absolute values. Then, the values are clipped to 2.0.
5. The normalized stamps are then concatenated with the integrity mask, ending up with a 6-channel image. When employing the Multiscale model, this process is repeated across four different scales, resulting in a 24-channel image.
6. Ultimately, the stamps are cropped or resized, depending on the model they will go into.

Beyond the preprocessing steps used in RJ23, we introduce new steps (highlighted in the red dashed box in Fig. 2) to incorporate the FFT calculation. Specifically, these steps are:

7. Starting from the complete (63×63 pixels) normalized difference image from step 5, we pad it to 128 pixels, filling with the median. The size of 128 pixels is chosen because the FFT algorithm is most efficient for dimension sizes that are powers of two.
8. We then apply the two-dimensional FFT and take the norm to obtain the amplitude.
9. Finally, we crop the central portion of the FFT. In our experiments, we kept the central 16×16 px region in all cases.

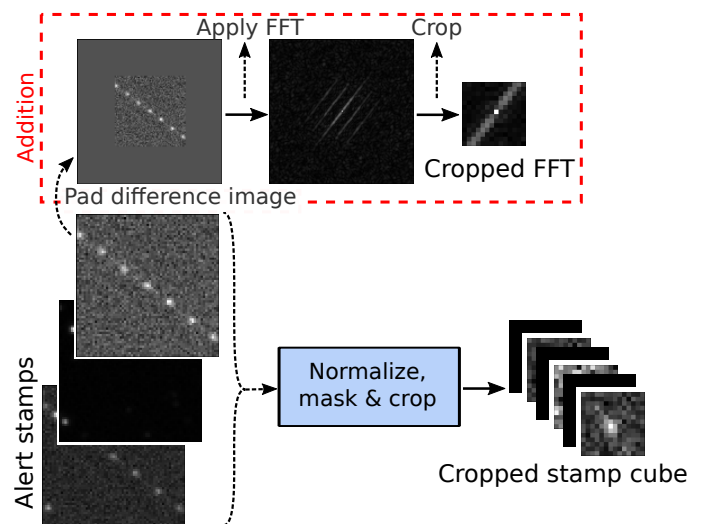


Fig. 2: Schematic of the preprocessing for our FFT-enhanced Stamp Classifier. The red dashed box encloses the new steps for the inclusion of the FFT with respect to previous versions of the classifier (e.g., RJ23).

There are two reasons to apply the padding, and both are associated with the nature of the FFT algorithm. First, since the transform maintains the sampling, padding allows increasing the spatial frequency resolution. Second, the FFT algorithm is constructed under the assumption that the sequence to be transformed is infinitely periodic. Since this is not the case for these

images, artifacts that might appear due to this inconsistency are mitigated by the padding. Similar measures are taken in other fields that use the FFT, such as computational Fourier optics, to deal with such issues (e.g., Voelz 2011). Although the FFT is a complex field, we focus on the amplitude due to the potential for data compression. Alternatives to this are discussed in Sect. 4.2.

2.2. Models

Fig. 3 illustrates the architecture of the models evaluated in this study. The key components include the cropped stamp cube, the FFT cutout from the preprocessing step, and additional metadata (primarily the coordinates of the alert). These inputs are processed through distinct neural network blocks before being combined in a final fully-connected layer that produces the model predictions.

In the architecture, the cropped stamp cube is passed through a convolutional block (referred to as the *Stamp convolutional block*) that applies rotational and flip augmentations. After the convolutional layers, the images are flattened, averaged over the augmentation steps, and passed through a dropout layer before being concatenated with the other features. While this block mirrors the structural design from RJ23, for the models that feature the FFT as an input (see the red short-dashed box in Fig. 3), the hyperparameters were re-optimized separately.

Parallel to this, the *FFT convolutional block* processes the FFT cutout. Similar to the Stamp convolutional block, it includes rotation and flip augmentation followed by convolutional and pooling layers, and finally, the output is flattened and concatenated with the other features.

To assess the value of incorporating the FFT block, we compared models that included it with those that did not:

- A. **Full:** The full $63'' \times 63''$ (63×63 px) FoV alert at $1''$ resolution is used. The input consists of three images (science, reference, and difference) and their corresponding integrity masks, creating a six-channel image.
- B. **Multiscale:** The stamp cube includes $8''$, $16''$, $32''$, and $63''$ FoV stamps at corresponding resolutions of $1''$, $2''$, $4''$, and $8''$. This produces a 24-channel image with four channels per image type.
- C. **Cropped-16:** The alert is cropped to a $16''$ FoV with the full $1''$ resolution.
- D. **Full + FFT:** Combines the full $63''$ FoV with the FFT block.
- E. **Multiscale + FFT:** Combines the multiscale stamp cube with the FFT block.
- F. **Cropped-16 + FFT:** Combines the cropped $16''$ FoV with the FFT block.

Model F (Cropped-16 + FFT) is particularly interesting due to its scalability. The amount of information in an image scales as the square of the number of pixels (N^2). However, the FFT algorithm's computational cost scales as $N * \log(N)$, making it significantly more efficient, especially considering the subsequent cropping of the FFT to retain only the most relevant information. This efficiency allows model F to capture better large-scale features of transient phenomena, such as satellite glints, while minimizing the inclusion of non-informative data (e.g., sky pixels in a science image) that would slow the pipelines.

For completeness, models D and E were also evaluated, although they did not show statistically significant improvements compared to models A and B. This is because the FFT block provided redundant information that was already captured by the

Table 1: Performance metrics for each model

Label	Model	F1 score (%)	Precision (%)	Recall (%)
A	Full	86.9 (0.6)	84.9 (0.8)	90.3 (0.3)
B	Multiscale	87.3 (0.3)	86.7 (0.4)	88.1 (0.5)
C	Cropped-16	85.8 (0.5)	85.3 (0.9)	86.6 (0.7)
D	Full + FFT	87.1 (0.5)	86.2 (0.8)	88.1 (0.5)
E	Multiscale + FFT	87.6 (0.2)	86.6 (0.4)	89.0 (0.2)
F	Cropped-16 + FFT	87.6 (0.4)	86.5 (0.7)	89.0 (0.6)

Notes. Mean values and standard deviations (in parentheses) are based on five training runs for each model.

larger FoVs in these models. The inclusion of the FFT block in these cases added complexity to the models, making them slower in both training and running.

2.3. Training

To ensure a fair comparison between models, we used the same dataset and adhered closely to the training procedures outlined in RJ23, including maintaining the same train-test-validation split. The training process involved a hyperparameter (HP) search using Ray Tune (Liaw et al. 2018), optimizing parameters such as the number of filters in the convolutional layers, learning rate, dropout rate, the size of the first convolutional kernel, and the size of the last dense layer.

For models A, B, and C (without the FFT block), we used the hyperparameters from RJ23. For models D, E, and F (with the FFT block), we performed additional optimization focusing on the FFT-specific convolutional layers. The search space for inherited parameters was narrowed to one-third of the original range, centered around the optimal values from models A, B, and C, while the FFT-specific parameters were searched within a broad range of values.

This approach ensured efficient HP optimization for the FFT models, with search times comparable to the non-FFT models. After identifying the optimal hyperparameters, each model was trained five times using the entire training set to compute the F1 score, precision, and recall (see Section 5.7.2. in Murphy 2012, for definitions), as well as to estimate their respective standard deviations and assess the significance of changes. The results are summarized in Table 1 for the test dataset.

3. Results

Table 1 presents the performance metrics for each model. As in RJ23, the Multiscale model outperforms the other non-FFT models. The inclusion of the FFT block in the Full model (A) did not affect the F1 score, indicating that the FFT, while increasing the complexity of the model, did not compensate with additional useful information. In the case of the Multiscale + FFT model (E), there were marginal improvements, primarily in distinguishing satellite glints from other types of bogus events that the large-scale, low-resolution channels of the Multiscale model could not resolve. In contrast, the Cropped-16 + FFT model (F)

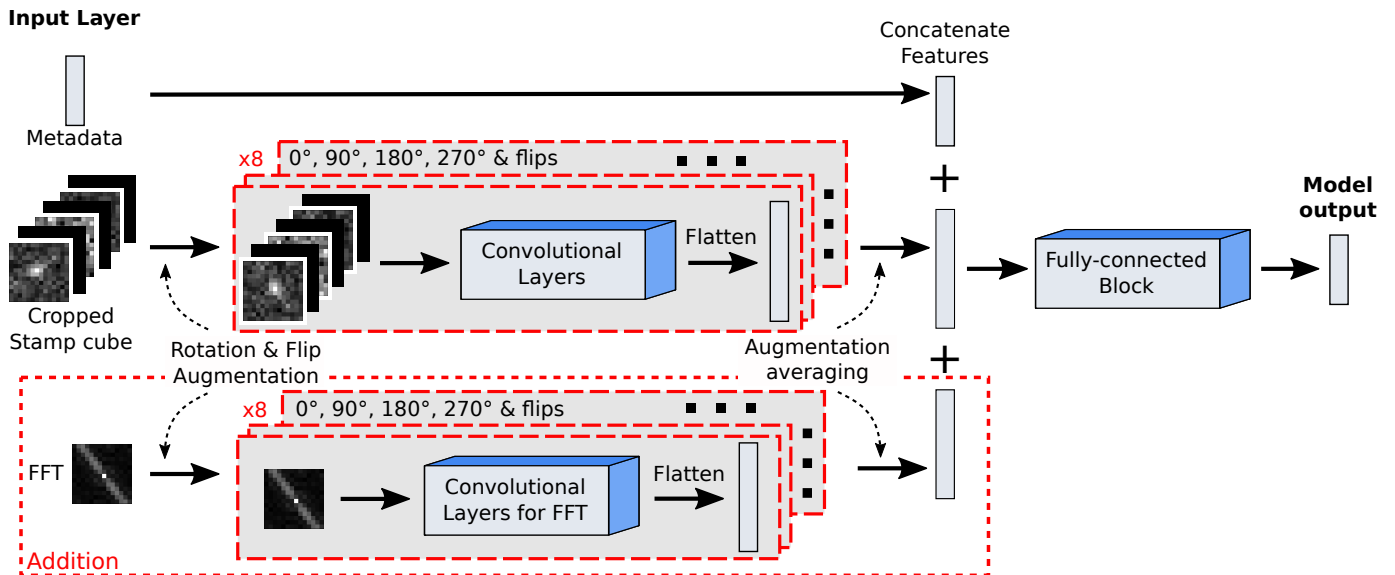


Fig. 3: A schematic view of the architecture of the ML models used in this work. The input includes the cropped stamp cube, the FFT cutout, and additional metadata. Both the stamp cube and FFT cutout undergo rotation and flip augmentation before being processed through separate convolutional blocks (red long-dashed boxes). The outputs are then concatenated with the metadata and passed through a fully-connected block for prediction. The red short-dashed box highlights the addition of the FFT block to the architecture, which was included in models D, E, and F (see Sect. 2.2).

showed significant improvements over Cropped-16 (C) across all metrics, indicating that inclusion of the FFT effectively enhances classification in this scenario.

Fig. 4 shows the confusion matrices for the Cropped-16 (C) and Cropped-16 + FFT (F) models. The addition of the FFT notably reduced misclassifications of satellites, bringing performance in line with models A and B as noted in Fig. 5. The detailed analysis of these results follows in the next section.

4. Discussion

We evaluate here the impact of incorporating the FFT in satellite detection and explore potential applications for internal survey pipelines responsible for generating transient alerts. By enhancing the early detection and classification process, FFT-based methods may help streamline the flow of high-quality alerts in large-scale surveys. We first analyze the experimental results before discussing broader implications.

4.1. The impact of the spatial frequency space

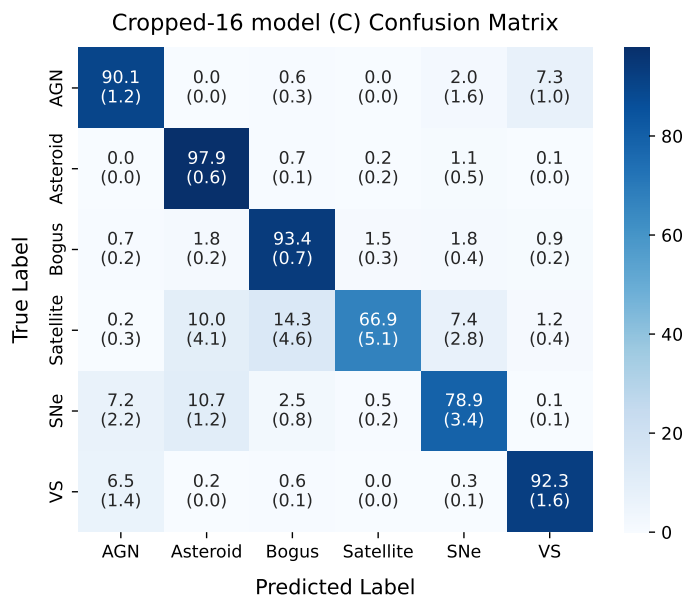
In Fourier space, the distinct signatures of satellites, characterized by transient and extended features, become clear. Satellite glints, challenging to detect in the spatial domain, are efficiently isolated in the FFT space, enhancing detection accuracy and providing a compact data representation for ML models.

To evaluate the benefits of FFT, we categorize image information into three types (source, context, and satellite), which correspond to different spatial scales and play a critical role in classification tasks. Source information captures small-scale, transient, or variable objects, such as the point-like SNe, AGN, or variable stars, or high proper motion asteroids such as near earth objects, which may look extended and trail across small angular distances, typically spanning only a few arcseconds in size. Context information provides larger-scale, unchanging environ-

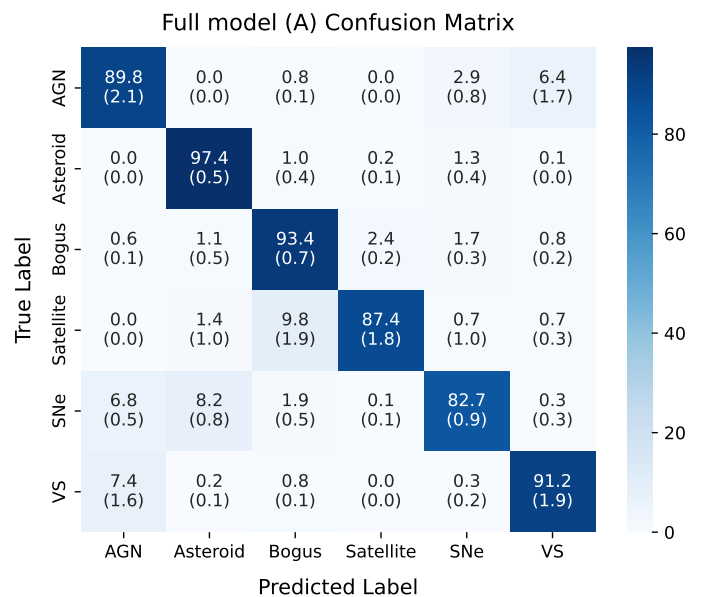
mental details, such as the position relative to nearby galaxies. The scale of this context information can vary; typical galaxy sizes range from a few arcseconds to several tens of arcminutes for extreme cases like the local Pinwheel Galaxy (M101). An important example is SN 2023ixf, discovered by amateur astronomer Koichi Itagaki (Itagaki 2023), within M101. Such a large host galaxy can complicate early classification efforts, as methods relying on context information, such as ALerCE’s Stamp Classifier (Carrasco-Davis et al. 2021), might miss SNe in such contexts, as happened in this case, where it was mislabeled as bogus. This underscores the importance of a multiscale approach for capturing crucial contextual data. Satellite information, however, is distinct due to its large linear spread and transient nature, making the FFT particularly effective in isolating it.

Our experiment showed that the Cropped-16 model (C) performed worse overall in the classification task compared to the Full (A) or the Multiscale (B) models (see Table 1). Since it contains less context information (smaller FoV), this is to be expected. It was particularly bad at identifying satellites, frequently confusing them with asteroids, SNe, and bogus detections (see below for more details). By including the FFT Block in the Cropped-16 + FFT model (F), these issues were largely resolved, with satellite identification improving enough to match the best performance metrics of the analyzed models. The confusion between satellites (true label) and asteroids, other bogus, and SNe was greatly reduced down to the level of the best-performing models. One issue that persisted was the confusion between SNe and asteroids, which was not improved by the FFT and did not match the performance of other models (see Fig. 5).

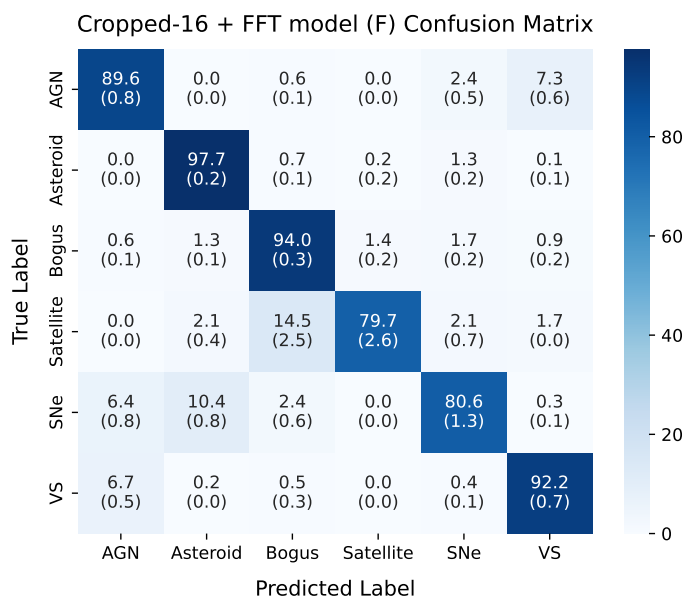
These results suggest that the FFT of the difference image is highly effective for identifying satellites and capturing the periodic nature of glints, which are challenging to detect in the spatial domain. However, compared to the Multiscale model, the FFT fails to provide the necessary context information for clas-



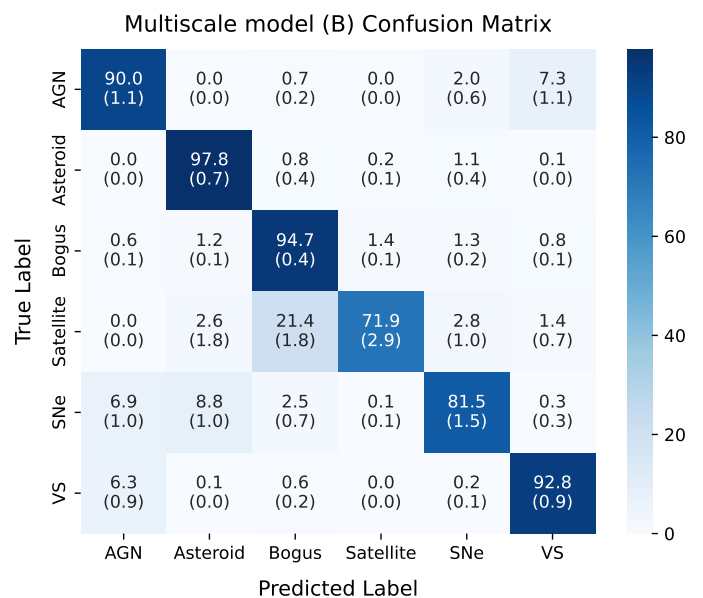
(a)



(a)



(b)



(b)

Fig. 4: Confusion matrices for the Cropped and Cropped + FFT models (C & F). The values are normalized by the True labels (rows). In parentheses are the standard deviations over 5 runs.

sifying some types of objects effectively, most noticeably in the confusion of SNe and asteroids.

It is important to note that the dataset is highly imbalanced, with significantly more bogus objects than satellites. To mitigate this, we employed balanced training batches and class-balanced cross-entropy loss for validation (see RJ23 for details). Despite these efforts, some class imbalance effects may remain. In this context, while the Bogus-Satellite confusion rate is the same for both models B (Fig. 5b) and F (Fig. 4b), Model F reduces Satellite-Bogus confusion by $6.9\% \pm 3.1\%$ compared to Model B. This highlights that Model F is distinctly better at distinguishing satellites from other bogus objects. Comparing model

Fig. 5: Same as Fig. 4 for the Full and Multiscale models.

F to model A (Fig. 5a), we find that Model F improves Bogus-Satellite confusion by $1.0\% \pm 0.3\%$, although Model A still outperforms Model F in Satellite-Bogus confusion by $4.7\% \pm 3.1\%$. Given the substantial class imbalance —with 27.5 times more bogus objects than satellites— these percentages should be interpreted cautiously. Overall, the 16" FoV Model F, enhanced by the inclusion of FFT, performs at least as well as, if not better than, the other models in satellite identification.

4.2. Future Prospects

In this study, we focused on the amplitude of the FFT, using it as a single additional channel for data compression. However, since the FFT provides a complex field, the phase information,

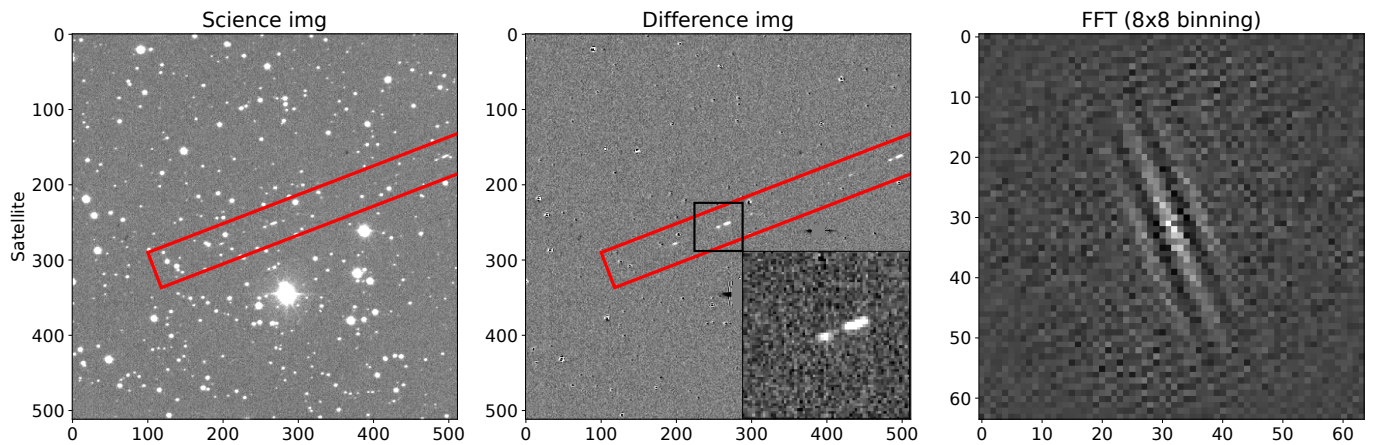


Fig. 6: 512×512 pixel cutouts from a ZTF full-chip image containing the alert-triggering object ZTF20aapfawc at the center. The satellite trail, highlighted with a red box, spans across the cutouts. Additional alerts raised by this satellite streak correspond to objects ZTF20aapfavz and ZTF20aapfavx, located $60''$ to the bottom-left and $250''$ to the top-right of the center, respectively, along the highlighted trail. The left and center panels display science and difference images, respectively, while the right panel shows the FFT of the difference image with an 8-pixel binning. In spatial frequency space, the satellite exhibits a distinctive fringe-like pattern, similar to the smaller stamps shown in Fig. 1.

though not considered here, may also prove valuable in distinguishing certain features. Future work could investigate alternative approaches, such as incorporating 1-channel real-part FFT or 2-channel real- and imaginary-part FFT components, to capture a wider range of spatial frequency features.

Beyond the technical aspects of the FFT, its practical applications in large-scale surveys like LSST are worth exploring. Integrating FFT into internal pipelines could significantly improve the identification of satellite contaminants before the data reaches downstream (alert) processing. However, it is important to note that for the FFT to be most effective, the satellite trail should be well-centered in the image. In our tests, an offset of 5 pixels already significantly distorted the signal, and larger offsets quickly led to the signal disappearance. Fig. 6 demonstrates the application of FFT over a larger cutout (512 px), beyond the typical 63 px of ZTF alerts. The central portion of the image focuses on a satellite trail, initially mislabeled as bogus but correctly identified as a satellite by our FFT-enhanced model, later confirmed by human inspection using the ALerCE Explorer⁴. Binning the FFT (right panel of Fig. 6) smooths out high-frequency details, allowing us to focus on large-scale variations that are more characteristic of satellite signatures. This approach demonstrates how FFTs could be implemented in internal pipelines, leveraging the information from very extended trails that produce apparently independent blobs at smaller scales, which may otherwise even fall below the detection threshold. Identifying and intelligently masking out these extended tracks could greatly reduce the number of complex satellite stamps which currently pass into the alert stream.

When comparing our method to other approaches for satellite detection, several distinctions arise. For instance, Karpov & Peloton (2022, 2023) used tracklet reconstruction to identify satellites by correlating non-repeating transient sources geometrically. While this is effective, and helped to reveal the impact satellites have on surveys, our method offers the advantage of considering both the bright and low-brightness features of satellite trails, which could become increasingly important as the LSST's deeper exposures reveal fainter satellite glints. Other ap-

proaches for detecting trails, mentioned in Sect. 1, involve analyzing images to search for elongated trail-like shapes (e.g., using the CREATETRACKIMAGE task from Laher et al. 2014) or employing CNNs (Duev et al. 2019b), similar to this work. Unconnected blobs from satellite glints pose a challenge for the former method. Regarding the latter, a promising area for future development might be to incorporate FFTs into it, given the relative ease to include FFT in ALerCE's Stamp Classifier.

However, it is important to acknowledge that no single method is likely to completely address the problem of satellite contamination. While we have highlighted the strengths of the FFT approach, reducing the misclassification of satellite events will likely require a combination of techniques, each addressing different aspects of the contamination problem. Combining methods with complementary strengths, such as tracklet reconstruction, trail detection, CNN-based models, and FFT-enhanced classification, should offer more robust mitigation of satellite contamination in large-scale surveys like LSST.

Another promising avenue involves trail-fitting techniques like those used by Vereš et al. (2012) for asteroids, which could potentially be adapted to include light-curve estimation. This could allow for the subtraction of satellite signatures from images. Such trail-modeling could be crucial for distinguishing between human-made and natural fast-moving objects, as well as broader space pollution characterization.

As of this writing, the public plans for the Rubin Observatory's data management facilities do not explicitly mention the use of graphics processing units (GPUs). However, given their widespread adoption in accelerating ML pipelines, GPUs would likely be a valuable addition to the survey's infrastructure, either from the outset or as a future upgrade. GPU-optimized FFT algorithms, known for their scalability and efficiency (e.g., see Moreland & Angel 2003; NVIDIA Corporation 2023; Advanced Micro Devices, Inc. 2023), offer an effective solution for processing the massive volumes of high-resolution data that LSST will generate. Their capacity for rapid FFT processing is essential to ensure that FFT-based feature extraction keeps up with the data flow in large-scale surveys like LSST. Incorporating GPUs into LSST's on-site computation facilities would significantly boost

⁴ <https://alerce.online/>

processing efficiency and scalability, though adapting existing pipelines to new hardware and software may pose challenges.

5. Conclusions

The study of transient astrophysical events in modern surveys such as ZTF and the LSST comes with several challenges, including managing the vast volumes of data and mitigating the presence of contaminants like CCD artifacts, template subtraction artifacts, and satellite trails. In the context of the burgeoning space industry, the latter is a rapidly growing problem that has yet to be adequately addressed by time-domain surveys (see, e.g., Catelan 2023, and references therein for a recent review). The current LSST bandwidth constraints on alert data volume may strongly limit the ability of downstream brokers and users to optimally filter out various contaminants. Thus, investigating efficient methods to improve the identification and filtering of contaminants early in the data stream, or alternatively to compress the data information more effectively into alerts, will hopefully ensure that the most scientifically valuable information is retained and leveraged by end users.

In this study, we explored the utility of the FFT in enhancing the detection of satellite glints within astronomical survey data streams and its potential as an image compression tool. We specifically utilized ZTF data, while also anticipating the challenges of the upcoming LSST era. Our results demonstrate that the FFT effectively isolates the distinct signatures of satellite trails and glints, concentrating these features in a compact region of Fourier space. This compactness allows for efficient data compression, significantly reducing the amount of non-informative data.

Our experiment compared the performance of ML models using FoVs of different sizes for the three ZTF alert image stamps (science, reference, difference) and assessed the impact of adding a central cutout of the FFT of the difference image as an input. As discussed in Sect. 4.1, incorporating the FFT block significantly improved the classification metrics of model C (which adopted a smaller 16'' FoV) to the levels achievable with the full 63'' FoV. In model F, using 16'' FoV stamps that included an FFT image, the overall F1 score increased to the level of the best performing models, with the most notable improvement on the classification of satellites. The confusion between SNe and asteroids, which can be the product of the small FoV, was not alleviated by the inclusion of the FFT. In this case, we found that the additional contextual information of larger FoVs was important, and the multiscale model introduced in RJ23 (model B here) did a better job while keeping the size of the input low.

Beyond the immediate scope of this work, the FFT's potential applications in internal data processing pipelines are vast. As discussed in Sect. 4.2, integrating FFTs into existing models can enable the analysis of larger image cutouts without a substantial increase in computational cost, facilitating more accurate and scalable contaminant detection. This approach could be particularly impactful for LSST, where efficient data handling and precise contamination filtering will be paramount.

Moving forward, this method opens several avenues for future optimization. For instance, since the signature of satellites in Fourier space is fringe-like, we found success in experiments to reduce the images into 1D arrays ("spectra"). The possibility of deriving features related to this 1D frequency space spectra or even coefficients that could capture the 2D nature may be of relevance as information to include in alert packets in these data streams. Additionally, integrating this approach with real-time

data processing pipelines could offer a substantial improvement in the purity and efficiency of alert systems, providing a more robust framework for upcoming large-scale surveys.

In conclusion, the FFT offers a powerful tool for both enhancing contaminant detection and improving data compression in astronomical surveys. By incorporating these techniques into future data processing pipelines, we can better prepare for the challenges of the LSST era and beyond, ultimately enabling more efficient and accurate astronomical research.

Acknowledgements. We acknowledge support from the National Agency for Research and Development (ANID) grants: Millennium Science Initiative ICN12_009 (FEB, AMMA, IRJ, MC) and AIM23-0001 (FEB, FF, MC), BASAL Center of Mathematical Modeling Grant FB210005 (FF, AMMA), BASAL projects ACE210002 (AB, MC) and FB210003 (JPC, FEB, AB, MC), FONDECYT Regular 1241005 (FEB), FONDECYT Regular 1231637 (MC), Beca de Doctorado Nacional (JPC). We also acknowledge the use of the Kultrún computing cluster at Universidad de Concepción, funded by Conicyt Quimal #170001, Anillo ACT172033, Fondecyt regular 1180291, Fondecyt Iniciación 11170268, Basal AFB-170002, and Núcleo Milenio Titans NCM19-058.

References

- Advanced Micro Devices, Inc. 2023, AMD rocFFT Library, version 1.0.29
- Bellm, E. C., Kulkarni, S. R., Graham, M. J., et al. 2018, Publications of the Astronomical Society of the Pacific, 131, 018002
- Carrasco-Davis, R., Reyes, E., Valenzuela, C., et al. 2021, The Astronomical Journal, 162, 231
- Catelan, M. 2023, in *Memorie della Societa Astronomica Italiana*, Vol. 94, 56
- Chen, X., Wang, S., Deng, L., et al. 2020, *ApJS*, 249, 18
- Cooley, J. W. & Tukey, J. W. 1965, *Math. Comput.*, 19, 297
- Duev, D. A., Mahabal, A., Masci, F. J., et al. 2019a, *Monthly Notices of the Royal Astronomical Society*, 489, 3582
- Duev, D. A., Mahabal, A., Ye, Q., et al. 2019b, *Monthly Notices of the Royal Astronomical Society*, 486, 4158
- Förster, F., Cabrera-Vives, G., Castillo-Navarrete, E., et al. 2021, *The Astronomical Journal*, 161, 242
- Graham, M. J., Kulkarni, S. R., Bellm, E. C., et al. 2019, Publications of the Astronomical Society of the Pacific, 131, 078001
- Itagaki, K. 2023, *Transient Name Server Discovery Report*, 2023-1158, 1
- Ivezić, Z., Kahn, S. M., Tyson, J. A., et al. 2019, *The Astrophysical Journal*, 873, 111
- Karpov, S. & Peloton, J. 2022, arXiv e-prints, arXiv:2202.05719
- Karpov, S. & Peloton, J. 2023, *Contributions of the Astronomical Observatory Skalnaté Pleso*, 53, 69
- Laher, R. R., Surace, J., Grillmair, C. J., et al. 2014, Publications of the Astronomical Society of the Pacific, 126, 674
- Liaw, R., Liang, E., Nishihara, R., et al. 2018, arXiv e-prints, arXiv:1807.05118
- LSST Science Collaboration, Abell, P. A., Allison, J., et al. 2009, arXiv e-prints, arXiv:0912.0201
- Masci, F. J., Laher, R. R., Rusholme, B., et al. 2019, *PASP*, 131, 018003
- Matheson, T., Stubens, C., Wolf, N., et al. 2021, *The Astronomical Journal*, 161, 107
- Moreland, K. & Angel, E. 2003, in *Graphics Hardware*, ed. M. Doggett, W. Heidrich, W. Mark, & A. Schilling (The Eurographics Association)
- Murphy, K. P. 2012, *Machine Learning: A Probabilistic Perspective*, Adaptive Computation and Machine Learning Series (Cambridge, Massachusetts, London, England: MIT Press)
- Möller, A., Peloton, J., Ishida, E. E. O., et al. 2020, *Monthly Notices of the Royal Astronomical Society*, 501, 3272
- Nordin, J., Brinell, V., van Santen, J., et al. 2019, *A&A*, 631, A147
- NVIDIA Corporation. 2023, NVIDIA cuFFT Library, version 12.6
- Patterson, M. T., Bellm, E. C., Rusholme, B., et al. 2018, Publications of the Astronomical Society of the Pacific, 131, 018001
- Perley, D. A., Fremling, C., Sollerman, J., et al. 2020, *The Astrophysical Journal*, 904, 35
- Reyes-Jainaga, I., Förster, F., Arancibia, A. M. M., et al. 2023, *The Astrophysical Journal Letters*, 952, L43
- Sánchez-Sáez, P., Arredondo, J., Bayo, A., et al. 2023, *A&A*, 675, A195
- Sánchez-Sáez, P., Lira, H., Martí, L., et al. 2021, *AJ*, 162, 206
- Smith, K. W., Williams, R. D., Young, D. R., et al. 2019, *Research Notes of the AAS*, 3, 26
- Tyson, J. A., Snyder, A., Polin, D., Rawls, M. L., & Ivezić, Ž. 2024, *ApJ*, 966, L38
- Vereš, P., Jedicke, R., Denneau, L., et al. 2012, *PASP*, 124, 1197
- Voelz, D. G. 2011, *Computational Fourier Optics*, Tutorial Texts (Bellingham, WA: SPIE Press)